Title

In search of a new photomolecular effect: evaporation of water exceeding the thermal limit

Permalink

https://escholarship.org/uc/item/0s55w8kk

Author

Ackerman, Alex

Publication Date

2023

University of California
Santa Barbara

In search of a new photomolecular effect: evaporation of water exceeding the thermal limit

A thesis submitted in partial satisfaction
of the requirements for the degree

Master of Science

in

Mechanical Engineering

by

Alexander McLeod Ackerman

Committee in charge:

Professor Bolin Liao, Chair
Professor Yangying Zhu
Professor Sumita Pennathur

September 2023

The Thesis of Alexander McLeod Ackerman is approved.

_____

Professor Yangying Zhu

_____

Professor Sumita Pennathur

_____

Professor Bolin Liao, Committee Chair

September 2023

In search of a new photomolecular effect: evaporation of water exceeding the thermal

limit

Acknowledgements

Curriculum Vitæ
Alexander McLeod Ackerman

Education

2023	M.S. in Mechanical (Expected), University of California, Santa Barbara.
2021	B.A. in Physics, University of California, Santa Barbara.

Publications

Y. Li, U. Choudhry, J. Ranasinghe, A. Ackerman and B. L. Liao, Probing surface photovoltage effect using photo-assisted secondary electron emission, Journal of Physical Chemistry A, 124, 5246, 2020.

U. Choudhry, F. Pan, X. He, B. Shaheen, T. Kim, R. Gnabasik, G. A. Gamage, H. Sun, A. Ackerman, D.-S. Yang, Z. Ren and B. L. Liao, Persistent hot carrier diffusion in boron arsenide single crystals imaged by ultrafast electron microscopy, Matter, 6, 206, 2023.

Abstract

In search of a new photomolecular effect: evaporation of water exceeding the thermal
limit

by

Alexander McLeod Ackerman

A recently-proposed photomolecular effect wherein polar liquids, principally pure wa-
ter, can be made to evaporate at higher rates than possible through thermal evaporation
alone under specific illumination conditions is experimentally investigated. Specifically,
measurements of water mass loss were taken while independently varying illumination
wavelength, intensity, angle of incidence and polarization. Prior experiments that re-
sulted in data supporting the existence of the proposed effect were duplicated in an effort
to obtain confirming results. Additionally, past experiments producing data consistent
with the proposed photomolecular effect were duplicated and extended to evaluate their
previously-unexplained results in the context of the photomolecular effect. An experi-
ment specifically intended to directly measure vapor generated by the photomolecular
effect was also conceived and built. The presented experiments ultimately failed to con-
firm or refute the existence of the proposed photomolecular effect, however qualitative
analysis of obtained results suggests that the effect is considerably weaker than previously
thought, depends on yet-unknown criteria, or possibly does not exist as expected.

Contents

Chapter 1

Introduction

The evaporation of water is a simple and well-understood phenomenon: thermal energy is absorbed, imparting kinetic energy to the molecules within the water causing them to escape the bulk liquid. From this understanding it follows that higher surface and bulk temperatures for the water correspond to higher evaporation rates. Heating of water via absorption of electromagnetic radiation is also well-understood as it is the primary means by which natural evaporation of water bodies occurs: sunlight is absorbed, heating lakes, rivers and oceans causing water to evaporate. The electromagnetic absorption spectrum of bulk water has been fully-characterized, with high absorption occurring primarily in infrared to radio frequencies. Bulk absorption of visible light has also been measured, with exceedingly low absorption coefficients of 0.00663 m^{-1} to 0.624 m^{-1} from 400 nm to 700 nm, with an average absorption depth in this spectrum exceeding 100 m [1]. The theoretical limit of mass lost to thermal evaporation $\dot{m}_{t,max}$ per unit area is given by

$$\dot{m}_{t,max} = \frac{q}{L + c_P(T_s - T_b)} \left[\frac{kg}{m^2 \cdot hr} \right],$$ (1.1)

where q is input power per square meter of surface area, L is the latent heat of vaporization, c_P is constant-pressure specific heat, T_s and T_b are surface and bulk temperatures of the water respectively [2]. For a bulk water temperature of $20°\,C$, a surface temperature of $20°\,C$ and solar flux $q = 1000$ W/m^2 the expected evaporation rate would be 1.45 kg· m^2· h. Evaporation rates as much as 10 times higher than this thermal limit have been experimentally observed for water contained within porous nanostructures and partially-dehydrated hydrogels under particular lighting conditions [3, 4, 5]. Furthermore, enhanced evaporation of water from both hydrogels and from free air-water interfaces has been observed with peak evaporation occurring under illumination from 520 nm transverse-magnetic (TM) polarized light at an incident angle of 30 degrees from the surface normal [6]. Contrary to conventional understanding of evaporation, these observations hint at the existence of a previously-undiscovered evaporation mechanism driven by the strong absorption of visible light by water at the air-water interface.

While latent heat reduction of water in porous structures offers a possible partial explanation of enhanced evaporation rates, differential scanning calorimetry (DSC) has shown a maximum latent heat reduction of only as much as 30%, which cannot fully account for rates 5 to 10 times higher than the calculated thermal limit that have been observed [2, 3]. Furthermore, latent heat reduction cannot explain the enhanced evaporation rates observed in free-surface experiments [6]. An alternative mechanism known as *photomolecular evaporation* has been proposed to explain the high evaporation rates observed under visible light illumination: water molecules can potentially be cleaved from the water surface at an interface by photons without undergoing the thermal evaporation process [2, 6].
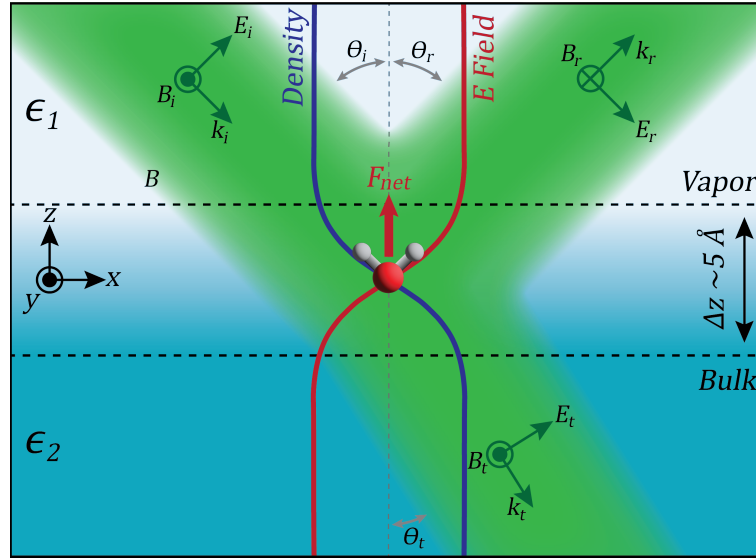
Figure 1.1: A TM-polarized beam originating in air with dielectric constant ϵ_1 propagates in the k_i direction towards a water surface where it meets the surface at an incident angle θ_i and is partially reflected at angle θ_r and partially refracted through the bulk water at angle θ_t. The bulk water has dielectric constant ϵ_2. Density at the interface changes over a distance of several Å; the dielectric constant also changes over this distance resulting in a large electric field gradient. The electric field gradient results in a net upward force on water molecules and / or water clusters within the transition region.

This proposed photomolecular evaporation effect relies on several conditions. First, it has been demonstrated that the density of water at an air-water interface changes over a finite thickness on the order of several Å [7]. Second, the refractive index of water vapor is dependent on the density of the water vapor, albeit only weakly [8, 9]. Third, the electric field perpendicular to the air-water interface is continuous as $\varepsilon_1 E_{\perp 1} = \varepsilon_2 E_{\perp 2}$ with ε_1 and ε_2 being the dielectric constants of air and water, roughly equalling 1 and 1.8 respectively [10]. These conditions imply that a steep electric field gradient is present across the air water interface. The force on each of the separated charges in a net-neutral polar molecule is $\mathbf{F} = q\mathbf{E}$; in an ordinary electric field the forces on the positive and negative ends of the molecule cancel, however in an electric field gradient the force at one end of the molecule does not cancel with the force at the other end, and a net force on

the molecule results [10]. This force is termed a "quadrupolar" force. Figure 1.1 depicts a conceptual view of the proposed quadrupolar force on a water molecule created by an incident beam at an air-water interface.
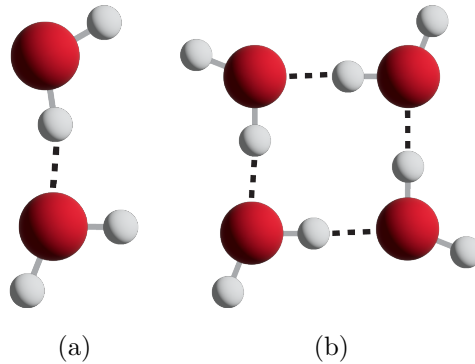

(a)   (b)

Figure 1.2: (a) Two water molecules bond together via a hydrogen bond (represented as a black dashed line) (b) an $n = 4$ water cluster

Another proposed contributing factor to the photomolecular evaporation effect is the formation of water clusters at the air-water interface [2, 6]. Water clusters are groups of water molecules linked together via hydrogen bonds. The existence of water clusters is widely accepted, however the exact details of the clusters is still a matter of open debate [6, 11, 12, 13]. Figure 1.2 depicts schematics of simple water cluster geometries.

There are two reasons why the existence of water clusters is significant to the photomolecular evaporation effect. First, molecular dynamics (MD) simulations have predicted that dipole moment is heavily dependant on water cluster size [14, 15]. This implies that forces acting on the water clusters resulting from the electric field gradient are greater than for individual molecules. Second, it is thought that a single photon may be able to break all bonds between a cluster and the bulk water, resulting in the ejection of many water molecules per incident photon [6].

1.1   Summary of Prior Research

Evaporation rate as a function of incident light wavelength, polarization and intensity has been measured for both porous hydrogels and free air-water interfaces. In these experiments, a sample of water or hydrogel floating on water was placed on a balance scale beneath a 100 W LED [2, 6]. LEDs with peak wavelengths of 390 nm, 420 nm, 520 nm, 590 nm and 65 0nm were used with a light pipe fabricated from 3M Enhanced Specular Reflection film to direct the light in a relatively narrow beam toward the sample container [6]. The incident angle of the light was varied from $0°$ (normal incidence) to $80°$ while intensity of the light varied from approximately 100 Wm^{-2} to 1500 Wm^{-2}. Evaporation was found to be linearly dependent on light flux, and peak evaporation at a given intensity was observed to occur for all wavelengths at incident angles between $30°$ and $40°$ [6]. Maximum evaporation was observed when water samples were illuminated by the 520nm LED, with measured rates at other wavelengths being significantly lower [6]. The experiment which produced these results consisted of a direct measurement of mass loss from a sample container illuminated by a light source of variable wavelength and incident angle [6]. Fundamentally this experiment is similar to the angled-beam experiment described in section 2.2.3. This experiment primarily differs from the angled-beam mass loss experiment described in 2.2.3 in that the former uses an incoherent, randomly-polarized light source while the latter uses a linearly-polarized laser source.

1.2   Motivation and Research Goals

The purpose of this work is to look for evidence to either support or refute the existence of the proposed photomolecular evaporation effect and to provide answers to the many questions surrounding the details of this effect. To achieve these goals three

experiments were devised. The first experiment sought to directly measure vapor lost as a function of time in response to a time-dependent laser source. The second experiment sought to measure mass lost to evaporation as a function of light intensity, incident angle and light polarization. The final experiment was designed to measure microscopic mass loss as a function of wavelength, intensity, polarization and incident angle.

The following chapters present detailed information on the realization of these experiments. Measurement results and analysis of results are also presented for each experiment.

Chapter 2

Vapor Absorption and Mass Loss Measurements

2.1 Vapor Absorption Experiment

2.1.1 Experimental Setup

The objective of this experiment was to measure time-dependent decreases in the beam intensity of an infrared probe resulting from the absorption of photons by water vapor generated by the interaction of a pulsed visible beam with an air-water interface. The vapor absorption experiment initially consisted of a ns-pulsed 515 nm green pump beam (Coherent model Flare NX 515-0.6-2) with a variable repetition rate and a continuous-wave (CW) 1064nm infrared probe beam (CrystaLaser model IRCL-700-1064). The pump beam was linearly polarized with a maximum pulse energy of 500 μJ at a repetition rate of 1kHz. The probe beam was also linearly polarized and had a maximum power of approximately 700 mW, with precise control of the power being performed by a combination of a zero-order half waveplate and a polarizing beamsplitter.

The probe beam was directed through a quarter waveplate to shift the polarization of the beam from linear to circular polarization. There were two reasons for doing this: first, circular polarization would eliminate the risk of detecting effects dependent on the polarization direction of the probe beam, and second, the circular polarization allowed for the probe beam to make two passes through the sample before being directed to a detector via the polarizing beamsplitter used for probe power control. The pump beam passed through a half waveplate used to rotate the orientation of the beam's polarization so that the beam was either S-polarized or P-polarized.

A quartz cuvette containing deionized water was placed atop a vertical translation stage, while the probe beam passed through a dichroic mirror into the sample cuvette. The vertical height of the water surface in the cuvette was adjusted using the translation stage so that the pump beam would intersect the air-water interface. The residual pump beam exiting the cuvette passed through a dichroic mirror and was dumped at a beam block. The probe beam was reflected off of the two dichroic mirrors to pass approximately 2 mm above the surface of the water while being centered above the axis of the pump beam. The probe was then reflected off of an IR mirror and directed through the sample in the reverse direction back to the polarizing beamsplitter and into a focusing lens and silicon photodetector (Thorlabs model PDA10A2). The power of the probe beam was adjusted such that it nearly saturated the photodetector. A 6 nm FWHM 1064 nm filter was placed in front of the probe detector to ensure no scattered pump light would be measured.

A second photodetector optimized for use in the lower visible spectrum (Thorlabs model PDA25K2) was placed in the path of a beam picked off from the pump and was used to generate the reference signal for a lock in amplifier (Sanford Research Systems model SR830). The IR detector's output was used as the input signal for the lock in amplifier. Figure 2.1a shows the layout of the vapor absorption experiment while figure
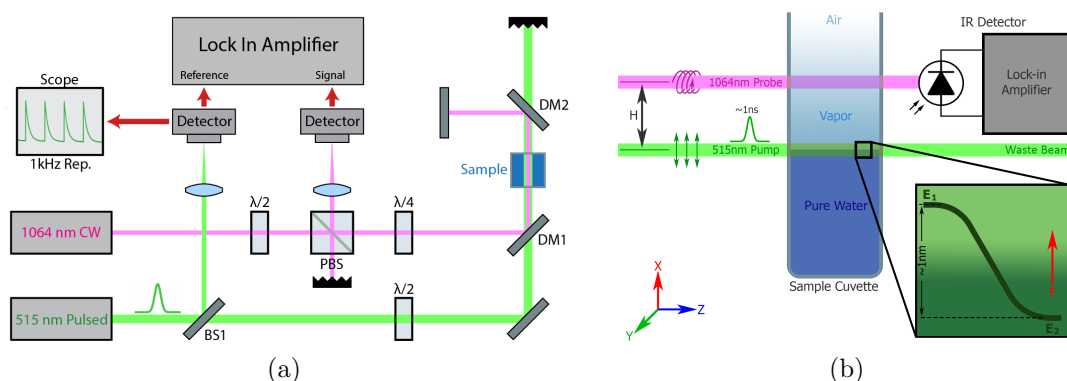
Figure 2.1: (a) Simplified Schematic of vapor absorption measurement experimental setup. A pulsed green pump beam passes through a half waveplate ($\lambda/2$) to control orientation of the beam's polarization. The beam then enters the sample cuvette parallel to and level with the surface of the deionized water. An infrared probe beam passes through a half waveplate ($\lambda/2$) and polarizing beamsplitter (PBS) for power control. The beam then passes through a quarter waveplate ($\lambda/4$) to convert the linearly-polarized beam to a circularly-polarized beam. The probe beam passes through the sample cuvette immediately above the pump beam and is then reflected back through the cuvette for a second pass in the reverse direction. The quarter waveplate converts the circularly-polarized beam back into a linearly-polarized beam and the polarizing beamsplitter reflects the probe into a detector. The signal from the detector is measured via a lock in amplifier using a reference signal generated from a sample of the pump beam. (b) cross section of pump and probe beams inside the sample cuvette showing the electric field gradient generated at the air-water interface by the pump beam.

2.1b shows a cross section of the pump and probe beams in the sample cuvette.

2.1.2   Experimental Results

No significant results were obtained from this experiment as the probe beam failed to produce a measurable signal. After initial testing with the pulsed 515 nm laser, the pump source was switched to a CW 532 nm laser with a nominal power of 200 mW (CrystaLaser model CL532-200-SO) modulated by a chopper wheel (Thorlabs model MC1F60) set to 1 kHz with a duty cycle of 50%. This switch was made as no signal was detected in the probe beam with either lock in amplifier or oscilloscope corresponding to the 1 kHz

repetition rate of the ns-pulsed laser. It was thought that the short, 1 ns pulse duration of the initial pump laser might have had insufficient duration to generate a significant amount of water vapor, however the modulated CW pump having a pulse duration of 500 μ S also failed to produce a measurable signal.

2.2   Mass Loss Measurement

2.2.1   Experimental Setup - Horizontal Beam

A 200 mW linearly-polarized 532 nm single longitudinal mode (SLM) laser (Crysta-Laser model CL532-200-SO) was used in this experiment. The laser beam passed through a half waveplate and polarizing beamsplitter for power control before passing through a second half waveplate for polarization orientation control. The beam was then directed through a pair of cylindrical lenses forming a single-axis Galilean telescope. The beam was expanded in the horizontal direction so that it was approximately 20 mm wide. The beam then passed through a 10 mm by 10 mm by 40 mm quartz sample cuvette, a 10 mm by 40 mm by 40 mm quartz sample cuvette or a 25 mm by 3 mm borosilicate sample dish filled with deionized water located atop a balance scale (Ohaus Scout model STX123). The beam was located such that the center of the beam intersected the surface of the water, and the wide beam ensured that the entire surface of the water was illuminated. Figure 2.2 shows a simplified schematic of the experimental setup. Figure 2.3 shows two of the sample containers used in the experiment with convex and concave surface menisci. The 25 mm diameter borosilicate dish (figure 2.3a) was filled such that the water's surface would be above the edge of the dish, while the quartz cuvettes (figure 2.3b) were filled so that the water level was considerably below the edge of the cuvettes.
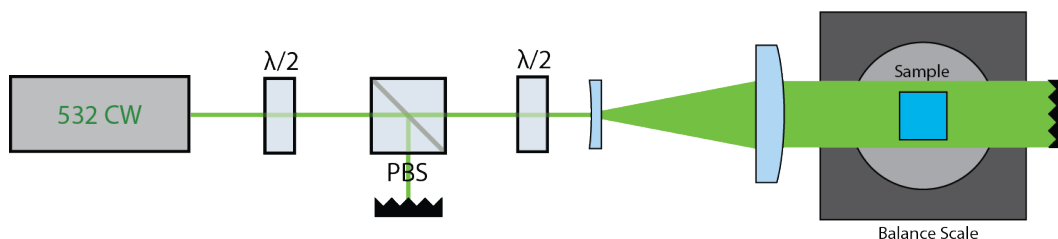
Figure 2.2: Simplified schematic of horizontal beam mass loss experiment. A linearly-polarized laser beam passes through a half waveplate and polarizing beamsplitter to control beam power, and then passes through a second half waveplate to control the orientation of the beam's polarization. the beam is expanded in the horizontal axis so that it intersects with the entire surface of water contained in a sample cuvette.

When the second half-waveplate was rotated such that the beam was S-polarized, an electric field gradient would be generated across the air-water interface. When the beam was P-polarized the electric field component of the beam would be parallel to the water's surface and no gradient would be present. The orientation of the beam parallel to the water's surface was chosen to maximize the electric field gradient, as the magnitude of the electric field component normal to the water's surface is proportional to the sine of the incident angle of the beam as measured from the normal direction of the water's surface.
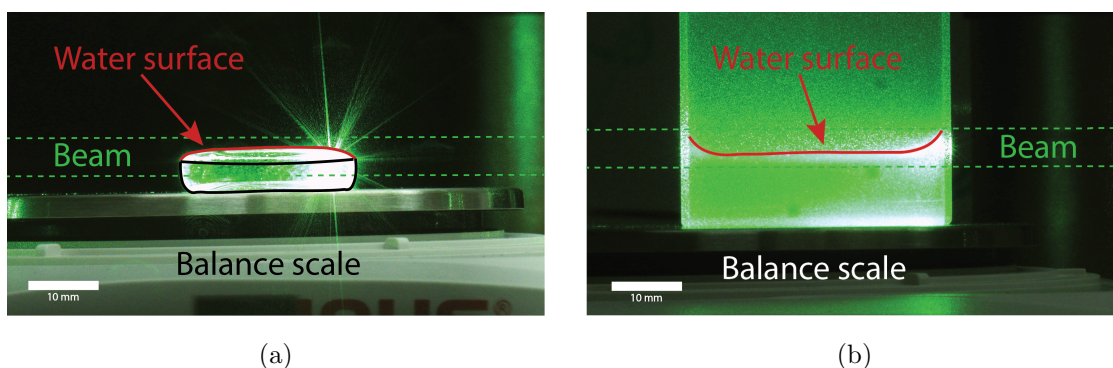

Figure 2.3: Side profile of sample containers used in the horizontal mass loss experiment. (a) A 25mm round borosilicate dish with a convex water meniscus (b) A quartz cuvette with a concave water meniscus.

2.2.2   Experimental Results and Analysis

This experiment did not produce meaningful results. As both this experiment and the aforementioned vapor absorption measurements both utilized beams parallel to the water's surface, it was hypothesized that a relatively large incident angle is necessary for the effect to occur despite the fact that the electric field gradient is greatest in the case of a parallel beam.

2.2.3   Experimental Setup - Angled Beam

A 2000 mW linearly-polarized 53 2nm laser (Civil Laser model LSR532H-2W) with a 3mm beam diameter was used for this experiment. The laser beam first passed through a polarizing beam splitter to ensure vertically-oriented polarization. The beam then entered a variable beam expander capable of expanding the beam by a factor of 2X to 8X before passing through a 2-lens Keplerian telescope to further expand it by a factor of 3. The final beam diameter was then clipped by a variable iris diaphragm, allowing only the center portion of the beam to pass through subsequent optics. The clipped beam was directed up a custom-fabricated periscope before being directed to a rotation stage-mounted mirror that would direct the beam downwards at a defined angle. The vertical orientation of the polarization ensured that there was a component of the polarization normal to the water surface for incident angles other than 0°. A small container of deionized water was placed in the path of the beam atop a triangular glass stand on a balance scale. The balance scale was coated with 3M Enhanced Specular Reflector (ESR) film to prevent the surface of the balance from heating up under laser irradiation. The purpose of the glass stand was to further isolate the water dish from any heat produced at the surface of the balance scale. The balance scale used was an Ohaus Pioneer PX225D with a resolution of 0.01 mg. Figure 2.4 shows a simplified

schematic of the experimental setup. Laser power was measured at the location of the water sample using a Newport 843R power meter and 919P-003-10 thermopile before beginning the experiment. A baseline natural evaporation rate was determined with the laser beam blocked by a manual shutter by measuring the mass lost over time spans of 30-90 minutes and performing a linear fit of the data. The laser was then unblocked for a period of 30-90 minutes and a new evaporation rate was determined as before. Finally, the laser beam was blocked again and the natural evaporation rate was determined once again.

The experiment was run with incident angles of 0° and 30°, the latter of which was found to be the angle of maximum evaporation in previous experiments [6]. Three water containers were used: a 25 mm diameter by 3 mm tall borosilicate dish, a 10 mm by 10 mm by 40 mm quartz cuvette and a 25 mm concave dielectric mirror on a BK7 glass substrate.
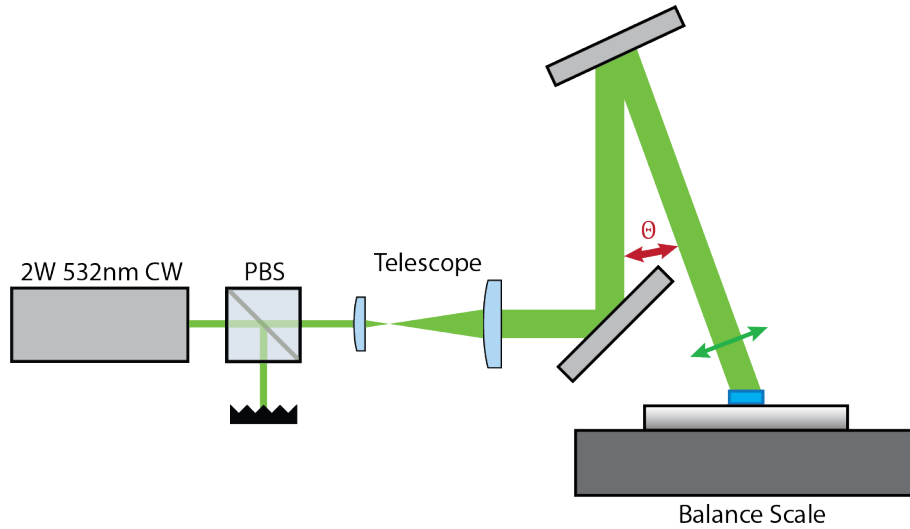
Figure 2.4: Simplified schematic of angled-beam mass loss experiment. A 2 W 532 nm CW laser emits a beam which passes through a polarizing beamsplitter (PBS) to ensure TM polarization. A telescope expands the beam to approximately 25 mm in diameter before the beam is directed via periscope onto the sample container at a variable angle of incidence θ. A balance scale directly measures mass lost over time with and without the beam irradiating the sample container.

2.2.4   Experimental Results and Analysis

Initial results were promising as they showed a clear increase in evaporation rate under laser illumination. A strong effect was only observed in cases where the incident beam diameter was greater than the diameter of the sample dish, i.e. the beam illuminated the dish perimeter as well as the contained sample. Thermocouple measurements revealed little to no change in sample temperature, so it was hypothesized that the proposed evaporation mechanism was not sufficient to explain the observed phenomena and a air-water-glass interface was necessary for the effect to occur. To this end, the experiment was repeated with the sample dish filled with DI water ans borosilicate glass beads in hopes that the increased surface area of the glass would lead to a stronger effect. While this did result in greater evaporation under illumination, the rate was largely independent of the polarization orientation of the light. Figure 2.5 shows the plotted data for both TE and TM polarization, with negligible difference between the illuminated evaporation rates. This observation suggests that something other than photomolecular evaporation must be occurring, and it was suspected that the rate increase was due to light absorption and heating of the glass sample dish causing a thin layer of water near the glass to become warmer than the bulk temperature and evaporate at a higher rate.
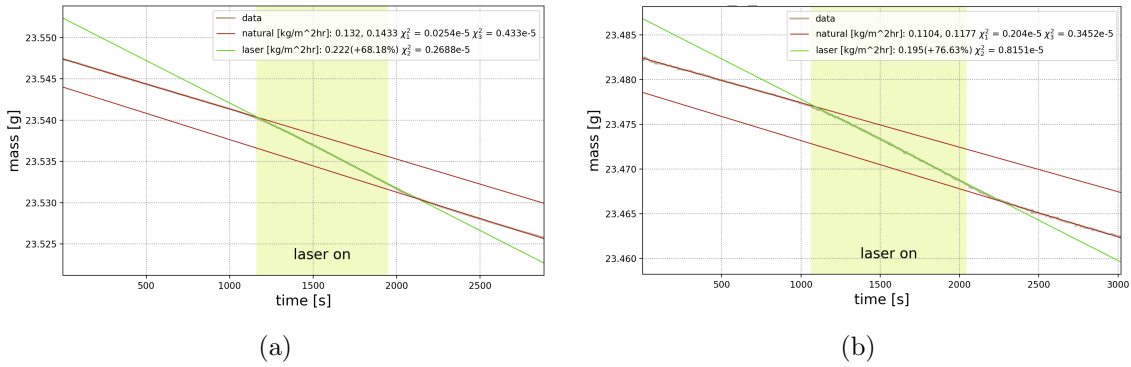
(a)   (b)

Figure 2.5: (a) Plot of mass loss with borosilicate beads in sample dish: incident beam has TM polarization, a 30° incident angle and 3000 W/m^2 flux. Room conditions: 61% relative humidity, 19°C. (b) Plot of mass loss with borosilicate beads in sample dish: incident beam has TE polarization, a 30° incident angle and 3000 W/m^2 flux Room conditions: 63% relative humidity, 19°C.

The earlier thermocouple measurements proved to be unreliable in detecting heating of the water's surface, so a thermal camera was used to monitor surface temperature over time. Figure 2.6 shows the average temperature change of an unfilled borosilicate sample dish under illumination at 532 nm with 3000 W/m^2 of flux. Without water present, the dish's average temperature rises by nearly a degree; with water present the edges of the dish absorb incident light and transfer heat into the water adjacent to the exposed edges of the dish.

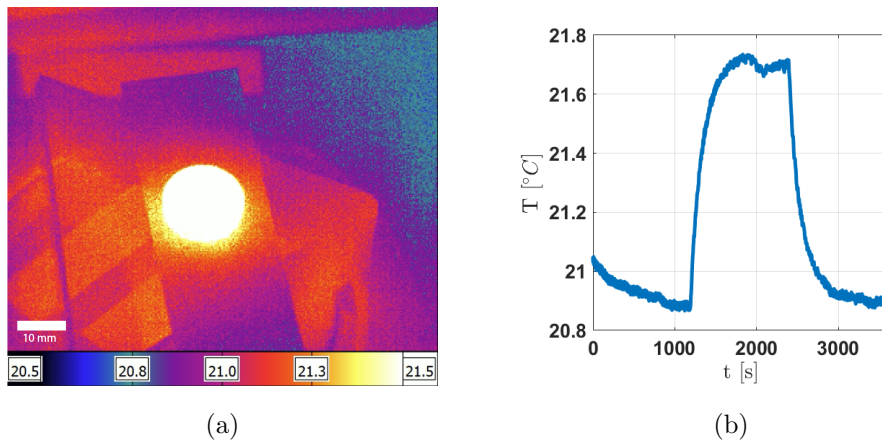(a)   (b)

Figure 2.6: (a) Borosilicate sample dish without water heated by laser irradiation. (b) Temperature change versus time of sample dish without water.

While the results of the thermal camera test clearly indicate heating plays a role in the increased evaporation rate, it does not rule out photomolecular evaporation as a component of the total evaporation rate. To reduce the evaporation rate due to heating of the sample container, the borosilicate dish was replaced with a concave dielectric mirror (Thorlabs CM254-025-E02) and DI water was placed inside the depression formed by the mirror's concave surface. The mirror had an estimated reflectivity of greater than 99% at 532 nm, and the mirror's N-BK7 glass substrate was estimated to absorb less than 8% of light transmitted by the dielectric coating. Based on these estimates the total worst-case absorption by the dielectric sample container was 0.08% of the incident light. While the total absorption by the borosilicate sample dish was not quantified, the dielectric mirror undoubtedly had lower absorption. The evaporation tests were repeated for both TE and TM polarization at flux values up to 6300 W/m^2. No significant change in the evaporation rate was observed for illumination under normal incidence or at 30°. Figure 2.7 shows the results of a test at 30° with a flux of 6300 W/m^2. It is clearly seen that the rate change is negligible between segments of the graph, and in fact the evaporation rate under illumination decreased slightly.
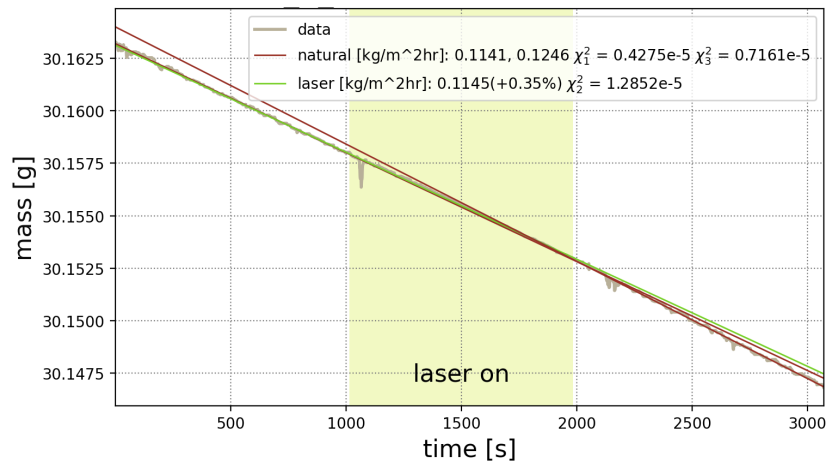
16

Figure 2.7: measured evaporation rates with laser illumination off, on and off again. A line was fit to each of the three rates for comparison of their average values. Negative spikes in the beige data plot are the result of table vibrations during testing and are not indicative of a rate change.

A thermal camera measurement was performed of the dielectric mirror under illumination both with and without DI water present in the dish. In both cases there was no observed temperature change. The observed temperature change of the borosilicate sample dish and the lack of an observed rate change with the dielectric sample dish both indicate that no photomolecular evaporation occurred during the course of this experiment.

Chapter 3

Quartz Crystal Microbalance Mass Measurement

3.1 Introduction

A quartz crystal microbalance (QCM) is a sensitive instrument enabling measurement of mass changes on the order of nanograms. The device consists of a piezoelectric quartz crystal between two electrodes that are connected to a Colepitts oscillator or similar. The QCM and oscillator circuit produce an output waveform with a typical frequency of several MHz. Such devices have been in use for decades in applications such as thin film deposition measurement and biological sample measurements [16].

The frequency shift ΔF of an AT-cut QCM is related to the change in mass Δm on the surface of the crystal through the Sauerbrey equation:

$$\Delta F = -\frac{2F_0^2}{A\sqrt{\rho_q \mu_q}}\Delta m,\tag{3.1}$$

where F_0 is the resonant frequency of the QCM's fundamental mode, A is the area of the

electrodes on the top and bottom surface of the crystal, $\rho_q = 2.65$ g·cm^{-3} is the density of quartz and $\mu_q =2.95\cdot10^{11}$dyn·cm^{-2} is the shear modulus of quartz [17], [16]. Equation 3.1 indicates a linear relationship between frequency and mass, and that a small decrease in mass on the order of nanograms will result in a relatively large increase in the resonant frequency of a QCM.

In a 2009 paper published in Analytical Sciences, authors T. Kawasaki, T. Mochida, J. Katada and Y. Okahata examine the effect of low-power s and p-polarized laser sources of various wavelengths on QCM sensors in atmosphere [18]. Kawasaki et al. placed a 27 MHz QCM with Au electrodes inside of a dark, controlled-humidity chamber and irradiated it with low-power lasers with wavelengths of 523nm, 636 nm and 785 nm [18]. The QCM was placed in a chamber with humidity controlled by saturated salt solutions placed in the chamber. High relative humidity causes adsorption of water molecules onto hydrophilic surfaces, whereas laser irradiation causes desorption of the water molecules on the surface of the QCM [18].

Kawasaki et al. varied laser power, angle of incidence and humidity and determined for each wavelength the frequency of the QCM increased linearly with power, with the rate of increase being dependent on the wavelength of the laser used [18]. It was found that the 532 nm green light produced the greatest change in frequency relative to input power, followed by the red 636 nm laser and finally the near-IR 785 nm laser [18].This trend might be explained by the tendency of gold to absorb shorter visible wavelengths, meaning that the increased frequency change rates for the short wavelengths are the result of thermal heating of the QCM.Varying incident angle from 0° to 90° resulted in decreasing ΔF with increasing angle for S-polarized light, and increasing ΔF with increasing angle up to a peak at around 70° before a rapid drop-off in the value of ΔF [18]. Increasing relative humidity was shown to linearly increase ΔF [18].

Previous publications conclude that the observed change in QCM frequency under

laser irradiation results directly from mass loss [19]. Kawasaki et al. propose the laser response of the QCM is due to a photo-induced surface reaction, though the specific details of this proposed mechanism eluded the authors [18].

3.2   Experimental Setup

A quartz QCM sensor was prepared by removing the lid from a commercially-available 6 MHz ECS-100AX quartz oscillator module. The contained crystal was 7.88 mm in diameter with a centered circular electrode 2.85 mm in diameter. It was determined through energy dispersive spectroscopy (EDS) that the QCM's electrode is comprised of pure silver. The oscillator was connected to a Keysight 53210A frequency counter which was then connected to a PC via USB and Keysight's BenchVUE software. The QCM was positioned so that a laser beam would be brought to a focused point on the center of the electrode. The power of the laser beam was controlled via the combination of a half waveplate and polarizing beamsplitter, while the orientation of the beam's polarization was controlled via a second half waveplate. The beam was split before the second waveplate to enable in-situ monitoring of beam power by a detector placed in the path of the second beam. Power of the primary beam was also checked at the sample location before every run of the experiment. The QCM crystal was placed atop a rotation stage to enable measurements to be taken over a range of incident angles. In all cases the laser beam was focused to a spot approximately 0.5mm in diameter at the center of the QCM's electrode. Laser sources used for the initial form of the experiment were a 2000 mW 532 nm diode-pumped solid state (DPSS) laser (Civil Laser model LSR532H-2W) and a 200 mW 589 nm sum-frequency generation DPSS laser (Civil Laser model LSR589HX-200). Measurements of frequency versus incident angle and polarization were taken under ambient temperature and humidity conditions, with temperature being be-

tween $19°C$ and $21°C$ and relative humidity between 50% and 55%. Measurements were obtained by beginning data collection with the 53210A to observe an initial oscillation frequency. The shutter was then opened to irradiate the QCM while data was being collected. Finally, the shutter was closed and data collection was ended after the QCM's measured frequency had returned to its initial value. For measurements at each incident angle polarization was rotated to generate both TM (P) polarization and TE (S) polarization, with 5 measurements being taken for each polarization. The reported results are the average of these measurements, and the error bars are the standard deviation of the measurements. Measurements of frequency versus beam power were collected by adjusting the applied beam power using the first half waveplate and measuring with a Newport 843R power meter and 919P-003-10 thermopile. For these measurements the QCM was positioned such that the incident laser beam was normal to the crystal surface. The change in frequency was then measured as before. Reported measurements indicate the maximum change in frequency versus measured beam power.
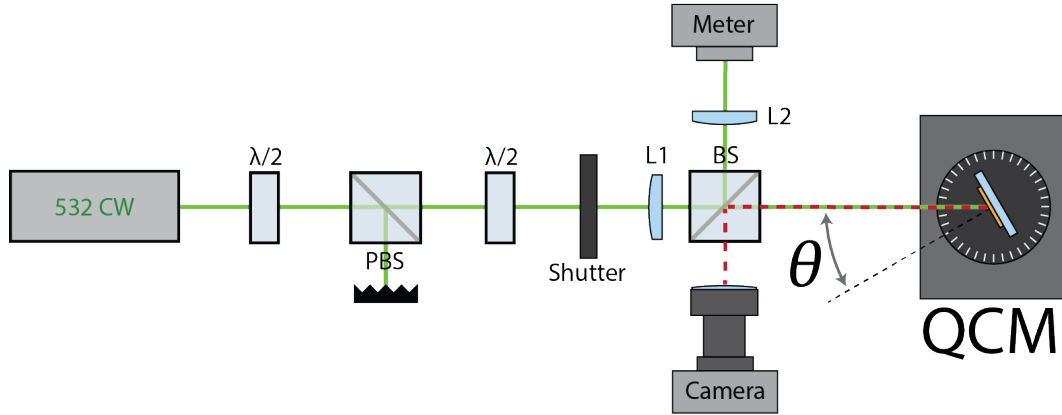
Figure 3.1: Simplified schematic of QCM experimental setup: A laser beam passes through a half waveplate ($\lambda/2$) and polarizing beamsplitter (PBS) enabling precise control over transmitted beam power. A second half waveplate enables control over orientation of the beam's polarization. A shutter blocks the beam for baseline frequency measurement, and a lens (L1) focuses the beam to a small spot on the QCM. A non-polarizing 50:50 beamsplitter (BS) divides the beam to enable in-situ power monitoring with a power meter and imaging of the laser spot on the QCM via a camera. The QCM is mounted on a rotation stage to control angle of incidence θ.

3.3   Experimental Results and Analysis

In all variations of the QCM experiment the shape of frequency change plotted against time remained qualitatively unchanged. Under initial laser illumination a rapid exponential growth dominates. Slow exponential frequency growth then occurs before the frequency reaches a steady state. When the laser is turned off the frequency initially decays rapidly on a similar timescale to the initial rapid growth, after which slow decay dominates before the frequency returns to its initial value. This trend was observed for all incident angles, wavelengths and polarization orientations. The increase in frequency over time resulting from laser illumination can be approximated by equation 3.2:

$$\Delta F = \Delta F_f \left(1 - C_1 e^{\frac{-t}{\tau_f}}\right) + \Delta F_s \left(1 - C_2 e^{\frac{-t}{\tau_s}}\right) \tag{3.2}$$

Where C_1 and C_2 are scaling constants, τ_f and τ_s are exponential time constants corresponding to fast and slow growth respectively. Figure 3.2a shows the general form of the observed plots, while figure 3.2b depicts the physical desorption stages that are thought to correspond to the observed plots.
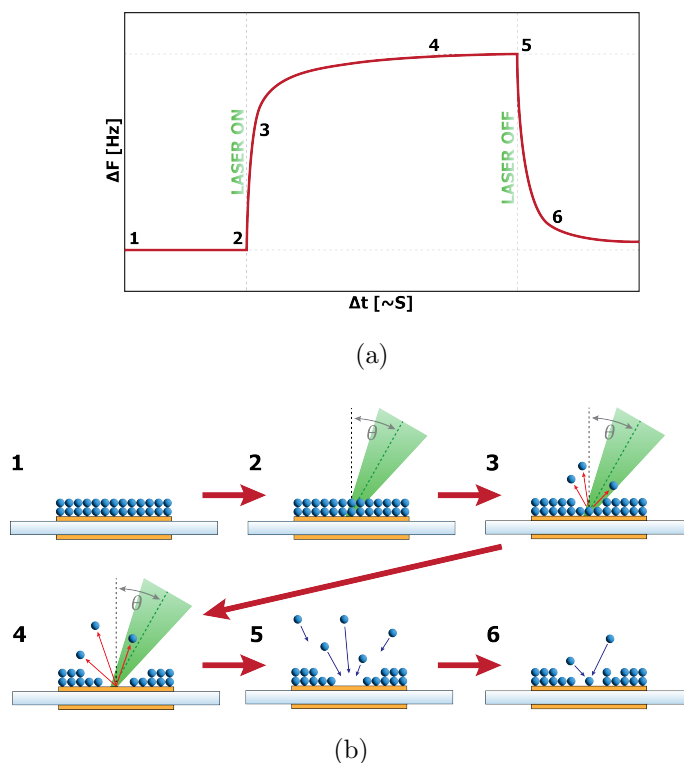

(a)

(b)

Figure 3.2: (a) Diagram of observed plot of frequency vs. time (b) conceptual diagram of desorption process on QCM sensor numbered to correspond with experimentally-observed regions of QCM frequency measurement plots. 1.) Laser is off, surface is coated with water molecules 2.) Laser is incident upon QCM surface 3.) A rapid exponential frequency change is observed 4.) Frequency change is dominated by slower exponential growth, approaches steady state 5.) Laser is turned off, rapid decrease in frequency is observed 6.) Frequency decrease shifts from rapid exponential decay to slow exponential decay

Fitting equation 3.2 to collected data predictably revealed that C_1 and C_2 depend on the optical power of the incident beam, the fits failed to show any correlation between the exponential time constants and optical power, wavelength or polarization. Time constants remained within an order of magnitude for all measurements. Any fluctuations

of time constants between tests were apparently random and were not repeatable for a given set of test parameters.
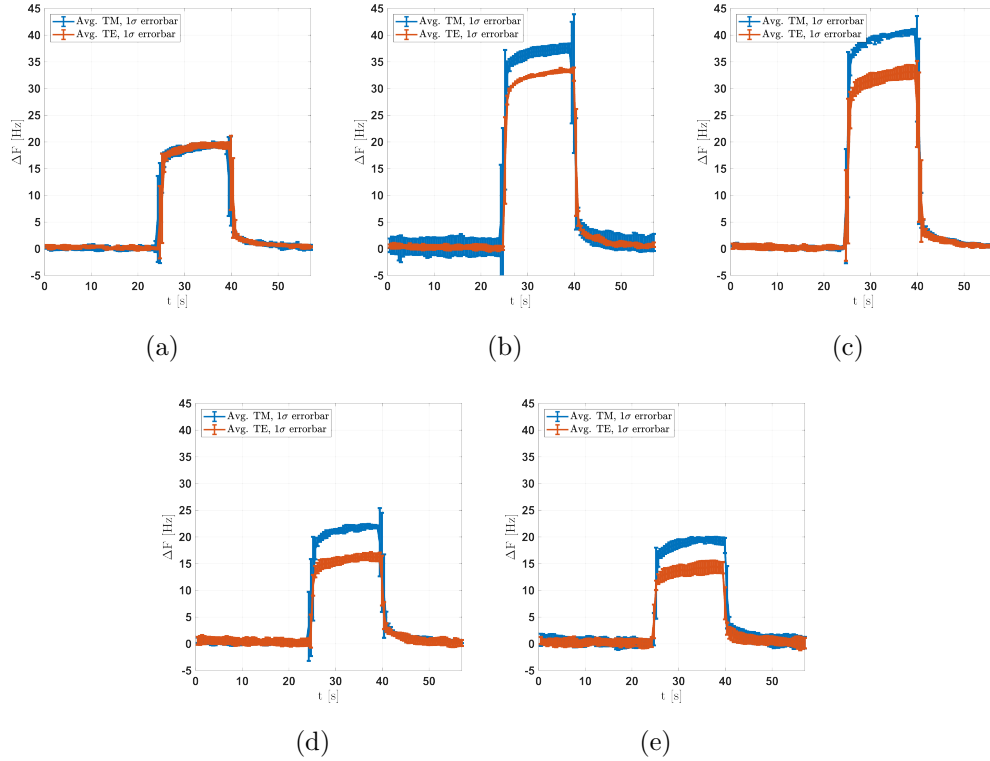

Figure 3.3: Averaged plots of 589nm TE and TM polarized light at (a) 0° incident angle, (b) 30° incident angle, (c) 60° incident angle, (d) 70° incident angle and (e) 80° incident angle.

Figure 3.3 shows measured frequency shifts resulting from laser illumination as a function of time. These measurements strongly indicate that there is a consistent, angle-dependent difference in frequency shift between TE and TM-polarized light.

A finer measurement of maximum frequency shift versus incident angle and polarization was performed next. Initial results with a 10 mW 532 nm laser focused to a 100 μ m spot at the center of the QCM indicated a correlation between incident angle and measured frequency shift as well as a correlation between polarization orientation and measured frequency shift. Figure 3.4 shows the measured frequency change of the QCM

as a function of incident angle for both TM and TE polarization. Under illumination by TM-polarized light the frequency shift was found to peak between 60° and 70°, while under illumination by TE-polarized light decreased with increasing angle from its maximum at normal incidence. While this result closely resembles the result obtained by Kawasaki et al., it is also similar in form to the accepted measurements of the absorption of TE-polarized and TM-polarized light by silver thin silver films as a function of incident angle [18].
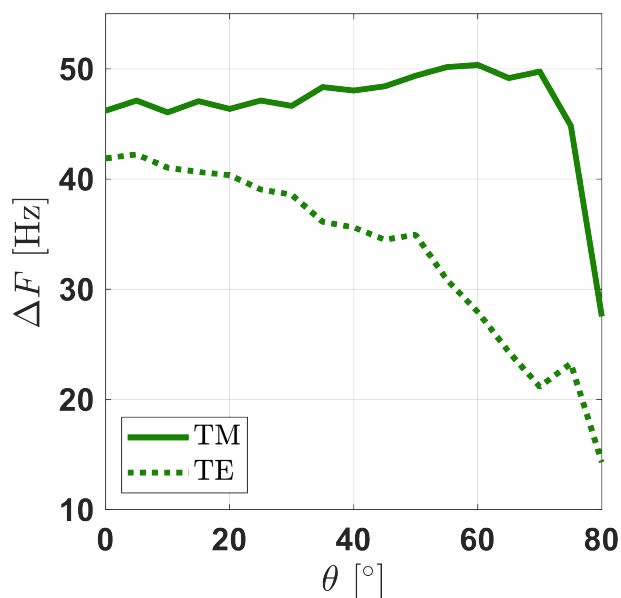

Figure 3.4: Frequency shift as a function of incident angle for TM and TE-polarized 532 nm laser light at 10 mW of power.

While the result of this first QCM experiment does not rule out a contribution to the QCM frequency shift from photomolecular evaporation, it cannot confirm it either. The similarity in shape of the measured curves to known absorption curves indicates that the primary effect observed is absorption related. There are two plausible explanations for this: either greater light absorption by the silver electrode at higher incident angles is causing water molecules to thermally desorb from the QCM thereby reducing the mass on the surface and creating a frequency shift, or the increased absorption and subsequent

heating of the silver film are directly driving a frequency shift in accordance with equation 3.3 below:

$$\Delta F_T = a_1 F_0 (T - T_0) + a_2 F_0 (T - T_0)^2 + a_3 F_0 (T - T_0)^3 ... \tag{3.3}$$

where T_0 is an initial reference temperature, $a1$, $a2$ and $a3$ are empirical constants determined by the QCM's crystal orientation [20]. For an AT-cut QCM crystal the linear and cubic terms dominate [20].

The most likely cause of the total observed frequency shift is a combination of thermal desorption and direct thermal frequency shift, with any photomolecular contribution being comparatively small. Direct thermal effects on the shift in frequency were estimated to contribute significantly to the total frequency change. This was demonstrated by monitoring the output frequency of the QCM during exposure to elevated temperatures. Furthermore, the manufacturer datasheet for the quartz oscillator used specifies a maximum frequency shift of 100 ppm per °C, meaning that the particular QCM used in the experiment would experience a maximum frequency shift of 60 Hz for a 1 degree temperature change. The experiment was always performed under ambient atmospheric conditions, so it is not possible to determine the precise thermal contribution to the total frequency shift. The presence of atmospheric water vapor in all tests means that desorption, whether it be thermal or photomolecular, and the resulting frequency change occurred in every measurement. Unfortunately, because the expected frequency shift resulting from photomolecular evaporation as a function of incident angle is expected to be similar to the shift resulting from light absorption and thermal heating, no conclusions supporting or refuting the existence of photomolecular evaporation can be made from this experiment.

In order to look for correlations between wavelength and frequency shift the exper-

iment was reconfigured to use laser sources of wavelengths varying from blue to red. Frequency shift versus incident laser power measurements at 45° and 60° were taken for all wavelengths with TE and TM polarization. Laser spot size and position were carefully matched between measurements via an imaging system in-line with the laser beam path. Laser power was adjusted to within a maximum of 1% error at 5, 10, 15, 20 and 25 mW for every laser. A linear fit was applied to the recorded data points for each wavelength and polarization. These fits are presented in figure 3.5a and b. The slope of each fit was plotted against wavelength in figure 3.5c and d.

A clear relationship between frequency and wavelength was not observed in this experiment, however it can be seen that for increasing wavelength the total frequency shift rate caused by incident TE-polarized and TM-polarized light decreases, and the difference in rates between TE and TM-polarized light tends to decrease. Interestingly, at an incident angle of 60° the difference in rates at 532 nm is large. This does not seem to be an outlier as the differences at 561 nm and 488 nm are both larger than the rate differences at wavelengths above and below them respectively. This does suggest a relative peak effect at 532 nm as predicted by Tu and Chen, however the peak occurs at 60° instead of the expected 30°, and the peak is relative between the two polarization orientations and not absolute as previously reported [2, 6].
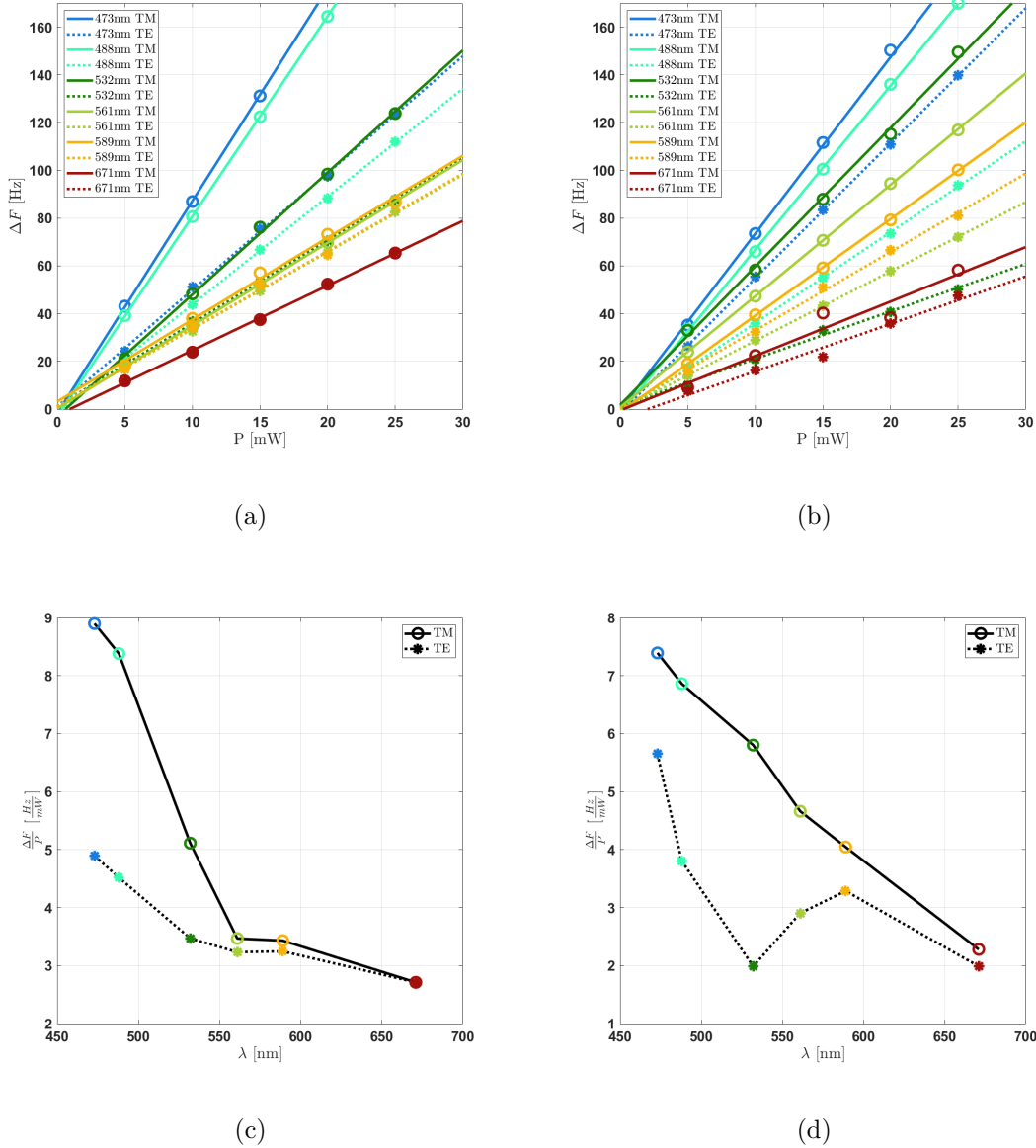
Figure 3.5: Frequency shift versus wavelength for (a) 45° incident angle and (b) 60° incident angle. Frequency shift rate versus light wavelength for (c) 45° incident angle and (d) 60° incident angle.

In the 45° incident angle plots the maximum rate is seen at the blue wavelengths with rates decreasing towards red. This is consistent with known absorption data for silver films and implies thermal effects are dominant. The 60° case is more interesting as it is

the only evidence in all of the presented experiments to indicate something other than thermal evaporation / desorption may be occurring under certain conditions. In spite of this, no conclusions can be drawn from this experiment.

Chapter 4

Summary and Outlook

Of the three presented experiments and their variations, all failed to produce a definitive result supporting or refuting the existence of the photomolecular evaporation effect. This primarily resulted from the inability to measure the effect independently from other effects, the inability to accurately quantify concurrent effects leading to mass loss and smaller than expected measurement results. Further refinements could be made to the experiments demonstrated in this work in an effort to obtain results of greater accuracy and precision, however the lack of obvious results across all experiments strongly implies that photomolecular evaporation is either not a real phenomenon, is far weaker than has been reported or depends strongly on additional factors that were not controlled or tested over the course of the experiments in this work.

The greatest evidence against the existence of photomolecular evaporation is the confirmed existence of thermal evaporation in the mass loss measurements caused by light absorption of sample containers. The Angled beam mass loss experiment was a modified form of the experiment performed by Tu and Chen from which most of the supporting evidence for photomolecular evaporation was produced. The version of the experiment built for this work was designed in consultation with the designer of the

original experiment and modified to utilize a laser source as opposed to an LED in order to eliminate long-wavelength infrared generated by the LED from reaching the sample. That this experiment failed to produce a result when light absorption was properly accounted for calls into doubt the validity of results from earlier experiments.

The QCM experiment largely produced data that is representative of the QCM's own properties, however the large gap between TE and TM-polarized light at 532 nm and a 60° angle of incidence hints at the possibility that photomolecular evaporation truly exists. This experiment failed to fully control all relevant variables, however. Factors such as slight changes in atmospheric humidity below the limit of what was recorded during each experimental run could have potentially impacted the results. Had this been controlled and ruled out it is possible that a firmer conclusion regarding photomolecular evaporation could be drawn.

The QCM experiment showed the most potential as it easily produced repeatable results that showed a clear dependence on the experiment's controlled variables. To fully investigate the photomolecular evaporation effect, aforementioned effects such as temperature and humidity need to be controlled. This could be achieved by placing the QCM in an environmental chamber where temperature and relative humidity could be easily controlled. This addition to the experiment was planned, but was not realized due to complexity and time constraints. Additionally, direct thermal effects on measured frequency need to be assessed. This could be done by baking the QCM at an elevated temperature to remove surface water before conducting the experiment in a vacuum chamber to ensure little to no water is present on the sensor. Finally, to rule out absorption effects of the QCM's electrodes, a custom QCM should be fabricated with an empty area in the center of each electrode such that the pure quartz substrate is exposed. The QCM should be treated to ensure a hydrophilic surface. This modification to the experiment should allow measurements to be taken without contamination of the signal

from electrode absorption.

The Vapor measurement experiment also shows merit, however the experiment as described and implemented in this work is not well-optimized. Ideally, the probe beam in such an experiment should be of a longer wavelength that is more readily absorbed by water vapor in order to produce the largest possible signal. Alternatively, the experiment could be configured to measure changes in the refractive index of the region immediately above the sample container. As water the pump beam ejects water from the surface, the region immediately above it would have an increased concentration of water vapor and hence its refractive index would change, albeit only slightly. This change could in principle be measured with a variety of arrangements: A Fabry-Perot Cavity with the sample placed inside, a Mach-Zehnder Interferometer, or perhaps with Schlieren Imaging. These methods are all highly-sensitive to small changes in refractive index, with the latter case commonly being used to visualize regions of air with increased water vapor concentration.

In spite of this work's experimental shortcomings and large uncertainty in measured values, it is likely that photomolecular evaporation does not exist, though this conclusion cannot be made confidently. Prior research exploring the photomolecular evaporation effect suggested that the effect was both large and easily observed. The experiments presented in this work did not produce results consistent with a large effect, nor did they consistently indicate that any effect was present under supposedly ideal conditions. Moreover, in experiments where mass lost to evaporation was measured, none of the evaporation rates exceeded the natural rates predicted for the conditions of the tests. More research is required to fully determine whether photomolecular evaporation is a real phenomenon or simply a result of unrealized experimental bias.

Bibliography

[1] R. M. Pope and E. S. Fry, *Absorption spectrum (380–700 nm) of pure water. ii. integrating cavity measurements*, *Appl. Opt.* **36** (Nov, 1997) 8710–8723.

[2] Y. Tu, J. Zhou, S. Lin, M. AlShrah, X. Zhao, and G. Chen *Photomolecular Effect Leading to Water Evaporation Exceeding Thermal Limit* (2022).

[3] F. Zhao, X. Zhou, Y. Shi, X. Qian, M. Alexander, X. Zhao, S. Mendez, R. Yang, L. Qu, and G. Yu, *Highly efficient solar vapour generation via hierarchically nanostructured gels*, *Nature Nanotechnology* **13** (2018), no. 6 489–495.

[4] Z. Dong, C. Zhang, H. Peng, J. Gong, and Q. Zhao, *Modular design of solar-thermal nanofluidics for advanced desalination membranes*, *Journal of Materials Chemistry A* **8** (2020), no. 46 24493–24500.

[5] H. Ghasemi, G. Ni, A. M. Marconnet, J. Loomis, S. Yerci, N. Miljkovic, and G. Chen, *Solar steam generation by heat localization*, *Nature Communications* **5** (2014), no. 1.

[6] Y. Tu and G. Chen *Photomolecular Effect: Visible Light Absorption at Water-Vapor Interface* (2022).

[7] J. Alejandre, D. J. Tildesley, and G. A. Chapela, *Molecular dynamics simulation of the orthobaric densities and surface tension of water*, *The Journal of Chemical Physics* **102** (1995), no. 11 4574–4583.

[8] P. Schiebener, J. Straub, J. M. Levelt Sengers, and J. S. Gallagher, *Refractive index of water and steam as function of wavelength, temperature and density*, *Journal of Physical and Chemical Reference Data* **19** (1990), no. 3 677–717.

[9] A. H. Harvey, J. S. Gallagher, and J. M. Sengers, *Revised formulation for the refractive index of water and steam as a function of wavelength, temperature and density*, *Journal of Physical and Chemical Reference Data* **27** (1998), no. 4 761–774.

[10] D. J. Griffiths, *Introduction to electrodynamics*. Cambridge University Press, 2017.

[11] F. H. Stillinger, *Water revisited*, Science **209** (1980), no. 4455 451–457.

[12] F. N. Keutsch and R. J. Saykally, *Water clusters: Untangling the mysteries of the liquid, one molecule at a time*, Proceedings of the National Academy of Sciences **98** (2001), no. 19 10533–10540.

[13] S. B. Lehmann, C. Spickermann, and B. Kirchner, *Quantum cluster equilibrium theory applied in hydrogen bond number studies of water. 1. assessment of the quantum cluster equilibrium model for liquid water*, Journal of Chemical Theory and Computation **5** (2009), no. 6 1640–1649.

[14] J. K. Gregory, D. C. Clary, K. Liu, M. G. Brown, and R. J. Saykally, *The water dipole moment in water clusters*, Science **275** (1997), no. 5301 814–817.

[15] J. Gelman-Constantin, M. A. Carignano, I. Szleifer, E. J. Marceca, and H. R. Corti, *Structural transitions and dipole moment of water clusters (h2o)n=4–100*, The Journal of Chemical Physics **133** (2010), no. 2 024506.

[16] Y. Okahata, K. Niikura, H. Furusawa, and H. Matsuno, *A highly sensitive 27 mhz quartz-crystal microbalance as a device for kinetic measurements of molecular recognition on dna strands*, Analytical Sciences **16** (Nov, 2000) 1113–1119.

[17] G. Sauerbrey, *Verwendung von schwingquarzen zur wägung dünner schichten und zur mikrowägung*, Zeitschrift für Physik **155** (1959), no. 2 206–222.

[18] T. Kawasaki, T. Mochida, J.-i. Katada, and Y. Okahata, *Laser response of a quartz crystal microbalance: Frequency changes induced by light irradiation in the air phase*, Analytical Sciences **25** (2009), no. 9 1069–1075.

[19] C. Egami, Y. Kawata, Y. Aoshima, H. Takeyama, F. Iwata, O. Sugihara, M. Tsuchimori, O. Watanabe, H. Fujimura, and N. Okamoto, *Visible-laser ablation on a nanometer scale using urethane–urea copolymers*, Optics Communications **157** (1998), no. 1 150–154.

[20] M. N. Rocklein and S. M. George, *Temperature-induced apparent mass changes observed during quartz crystal microbalance measurements of atomic layer deposition*, Analytical Chemistry **75** (2003), no. 19 4975–4982.